Energy Optimal Flight Path Planning for Unmanned Aerial Vehicles in Urban Environments Considering Trajectory Uncertainties

H. Rienecker* and V. Hildebrand† and H. Pfifer‡
Chair of Flight Mechanics and Control, Technische Universität Dresden, Dresden, 01062, Germany

This paper introduces a comprehensive approach for computing energy-efficient flight trajectories for unmanned aerial vehicles (UAVs) while considering trajectory uncertainties. The specific locations and environmental conditions under which the UAV will operate are inherently uncertain. Our goal is to minimize the sensitivity to these uncertainties in order to mitigate potential energy losses. The primary optimization objective is to minimize energy consumption by exploiting local wind phenomena, while accounting for negative effects of drift and turbulence. The flight path planning algorithm uses a precalculated time-averaged wind field to optimize the flight path and a time-dependent wind field to account for turbulent airflow dynamics. To address the optimization sensitivity to uncertainties, a specialized cost function is integrated into the A-star Algorithm, a type of branch-and-bound optimizer. Three distinct uncertainties are independently established for optimization: local drift, reduced upwind due to vortices, and turbulence avoidance. The key strategies applied address these uncertainties to achieve energy-efficient flight paths with reduced sensitivity. The proposed approach is demonstrated using a benchmark scenario involving a delivery UAV. Optimized flight trajectories are compared against shortest path trajectories. The results demonstrate significant energy saving potential when flying in urban areas by exploiting knowledge of the current wind conditions and minimizing the effects of uncertainties.

I. Introduction

In urban environments, the field of last-mile logistics currently faces significant challenges. Increasing traffic congestion and space usage demand innovative solutions. Especially, the final step of the supply chain is often the least efficient. However, electrically powered unmanned aerial vehicles (UAVs) present a promising solution for improving last-mile logistics, even in remote areas, while minimizing environmental impact. This paper is driven by the expanding integration of delivery UAVs into urban environments for last-mile logistics. Delivery UAVs have the capability to alleviate urban street traffic and reduce delivery times. Furthermore, their degree of automatization and fully electric propulsion make them cost efficient and environmentally friendly. In general, UAVs have lower payload capacities compared to ground-based vehicles [1] and optimizing their efficiency is highly important. A proven strategy to increase energy efficiency is to optimize the flight paths. In previous research [2–4], we demonstrated that exploiting wind conditions in urban areas inside the path optimization can significantly reduce the power consumption for typical delivery missions.

However, uncertainties in environmental conditions and deviations from the trajectory can negatively impact the actual gains. The common uncertainties considered in path planning for UAVs are weather uncertainties [5–7] or GPS accuracy [8]. Among the most prevalent uncertainties are wind-related factors. Altering wind conditions, induced by gusts and inadequate trajectory-following control, can result in deviations from desired aircraft positions. Numerous strategies have been developed to treat these uncertainties in research. One such strategy involves the implementation of predefined buffer zones to avoid conflicts among multiple aircraft using the same airspace [5]. Moreover, innovative approaches have been explored to handle uncertainties in wind magnitude and direction. For instance, probabilistic path planning methodologies have been applied to Montgolfiere balloons navigating the atmospheric conditions of Saturn's moon, Titan [9]. Similarly, Gaussian distributions have been used to model uncertainty in time-varying wind fields, with the aim of minimizing UAV energy consumption through wind-energy exploitation [10]. A study conducted by

*Research Associate, Chair of Flight Mechanics and Control, hannes.rienecker@tu-dresden.de
†Research Associate, Chair of Flight Mechanics and Control, veit.hildebrand@tu-dresden.de
‡Professor, Chair of Flight Mechanics and Control, harald.pfifer@tu-dresden.de

Kay et al. [11] investigated the impact of turbulent flow on UAV wing performance, prompting considerations to avoid excessively turbulent areas where reduced performance may occur. Wang et al. [12] further specifies the influence of environmental factors, such as constant wind, turbulent flow, various types of wind shear, and propeller vortex, on UAV operations in low-altitude environments. Simulation tests were conducted to assess the effects of different wind conditions on UAV trajectories and flight dynamics, revealing potential instabilities in flight states. Consequently, it was advised to steer clear of areas presenting hazardous conditions.

The present paper addresses this issue by obtaining energy-efficient flight paths which are less sensitive with respect to the uncertainty of the actual flight. The previous studies identified three main sources of uncertainties heavily impacting the actual performance. The first source is a local path offset also referred to as drift. It results in a change of the encountered wind conditions and reduces the actual energy savings. The second uncertainty type is the temporal variability of wind in an urban environment due to turbulent airflow. It requires an examination of scenarios where the UAV encounters worse wind conditions than those represented by the time-averaged data considered in our previous research. The last uncertainty source is the explicit consideration of turbulence in the optimization to circumvent regions characterized by severe changes in wind velocities. Our preceding methodology is extended to address the three main sources of uncertainties during the actual operation of the UAV. All three uncertainty effects are individually incorporated into the optimization to yield a trajectory which is less sensitive to perturbations.

This paper is organized into four sections. In section II, we introduce a realistic city district representative of a typical European area, which was developed in our previous work [3]. This city district comes with a realistic wind field for the urban environment that was derived using a Parallelized Large-Eddy Simulation Model (PALM) [13]. The determined wind field was substantiated through validation conducted in a wind tunnel experiment [14].

Thereafter, we provide an overview of our approach to achieving energy-optimal flight path under various wind conditions. Section III describes our customized A-star algorithm, specifically designed to address the challenges of energy-efficient path planning in urban environments. This algorithm builds upon the basic A-star algorithm, a widely used method in trajectory optimization. Prior research [15, 16] demonstrates the applicability of the A-star algorithm in trajectory optimization, with variants such as Theta-Star also being explored [17, 18]. The customized algorithm in this paper accounts for the turning constraints of the UAV and integrates smoothing techniques to generate flyable trajectories directly during the optimization process. Path smoothing is achieved by applying piecewise polynomials that ensure a continuous trajectory within the limits of the UAV's flight envelope. Specifically, continuous cubic Bézier spiral segments, as derived in [19], are employed to satisfy the maximum curvature constraints of the UAV.

The main aspect of this paper is the consideration of the uncertainties. In Section IV, gusts are treated as follows: Undetermined horizontal gusts cause local drift. Consequently, the effects of lateral displacement from the intended trajectory within a specified distance were examined, taking into account deviations both to the left and right of the desired track. Eddies introduce variability in upwind conditions, which is the primary factor influencing energy required. Hence, the emphasis of this approach is on mitigating upwind effects. Finally, in the last approach, turbulence is quantified, with a higher penalty factor indicating a greater need for avoidance. The feasibility of incorporating combinations of two out of the three sensitivity factors is demonstrated as a viable feature.

We apply a realistic city district connected with the generated wind field and apply the path optimization methodology, which includes flight trajectory modelling and their sensitivities. The effectiveness of the proposed approach is demonstrated through two delivery tasks, where the energy-optimized paths including the sensitivities in the optimization process are compared to the shortest routes and the energy-optimized paths without the sensitivities in Section V.

II. Urban Logistic Scenario

In typical last-mile logistics scenarios, unmanned aerial vehicles (UAVs) are used to transport goods within designated area of a city. This involves the UAV flying from a pick-up point to a drop-off point, powered by a fully electric fixed-wing aircraft. The aircraft examined in this example is comparable in size and characteristics to the Phoenix Wings PWOne delivery UAV [20], which has a wingspan of 1.3 m and a maximum take-off weight of 3.4 kg. Operating at an average cruising speed of 60 kph, the UAV is estimated to have a glide ratio of $G = 16$.

The generic city model and its wind field are adopted and validated from previous work [3, 14]. The model represents a typical European urban area and comprises eight buildings of unique shapes and varying heights, as depicted in Figure 1. Specifically, the model includes three residential buildings with a height of 50 m, four terraced houses with a height of 20 m each, and a supermarket building with an attached office block reaching 15 m in height. This arrangement was designed to capture typical local wind effects found in urban environments. By exploiting these wind fields, we can

potentially decrease the energy consumption of an UAV during a delivery mission.

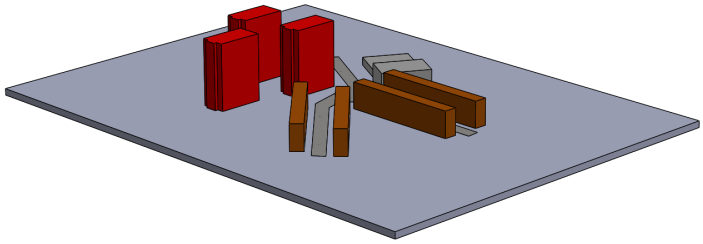

Fig. 1 Generic city model that represents a typical European urban area for simulating delivery tasks

This paper examines two distinct test scenarios involving two delivery tasks under a consistent wind speed. As illustrated in Figure 2, these scenarios use a single wind direction across all cases to remain within the influence zone of high-rise buildings. The delivery tasks involve flying from Point South to North and East to West. The primary objective in each scenario is to minimize the energy consumption of the UAV by taking advantage of local wind effects. Thereafter, trajectories were computed to account for sensitivity to drift, turbulence, avoidance of turbulent areas, or a combination thereof. Subsequently, these trajectories are compared based on their energy requirements and sensitivity. We assume the aircraft maintains a constant true airspeed corresponding to its best-performance cruise speed. The starting and ending altitude is set at 20 meters, a realistic altitude for air delivery in urban areas where takeoff and landing occur in multicopter mode. The energy required for these procedures is not taken into account. The investigation is based on average wind speeds typical of European cities, with Dresden, Germany serving as a representative example. Three characteristic wind speeds at a height of 10 meters were selected to represent the wind speed spectrum, as detailed in our previous paper [3]. Exemplary, we selected the calmest day for the following investigation. The day-averaged wind speed was used to construct a wind profile shape derived from a wind tunnel experiment described in [21]. Hence, the freestream wind speed is $u_{W\infty} = 6.5\,\mathrm{m/s}$ for the wind profiles.

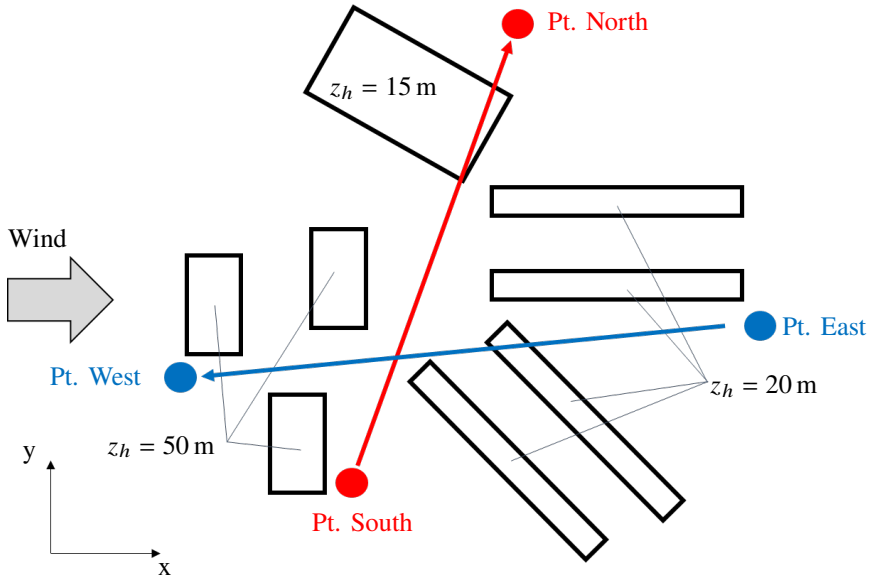

Fig. 2 Flight scenario with constant wind direction from west, as well as two tracks by flying from Point East to West and South to North

The topography of the generic city model and the realistic wind field were applied to a large eddy simulation (LES) to generate an accurate representation of the wind field within the urban environment for subsequent flight path

optimization. Further description regarding the software used, its configurations, and validation procedures can be found in [3]. The LES was conducted over a simulated time period of 4 hours. From this simulation, two datasets were extracted to serve as input for the path optimization process. The wind data from the final simulated hour is used to compute both the average wind data and the time-dependent wind data for the last minute. Therefore, Turbulence was modeled based on the standard deviation of the time-dependent wind components at each LES vertex after simulation. The equidistant grid points generated by the LES were also used to establish a waypoint system by connecting nearby vertices. This waypoint system enables pathfinding for the aircraft, allow it to fly from its current vertex to neighboring ones. Moreover, our approach entails evaluating furhter adjacent node connections to allow for greater directional possibilities inspired by the concept of increased connectivity [17]. However, increasing connections can lead to longer computational times. In our implementation, we have used connectivity to the waypoints of the three adjacent cells as a trade-off between the quality of headings covered and computational efficiency, resulting in a more winding path. Additionally, the vertical grid was supplemented with waypoints to accommodate flight paths tailored to the UAV's flight performance, as described in [4] clearly.

III. Trajectory Optimization

The aim of flight path planning is to minimize a cost function, denoted as J. This cost function represents the energy required for the UAV, and optimizing it provides an energy-optimal flight path. As previously mentioned, a tailored version of the A-Star-Algorithm is used to optimize routes or trajectories from a start to an end point. This algorithm is built upon the basic A-Star-Algorithm widely used for pathfinding tasks. In this paper, we offer a brief explanation of the basic A-Star-Algorithm and our customized version. Furthermore, we introduce an enhancement in the subsequent section that addresses uncertainties influencing the energy required.

In short, the A-Star Algorithm is initialized at a start point. Then, it navigates to the end point determining the optimal path by selecting the most favorable point at each branching. The best point is identified by the lowest total cost of the path, computed as the sum of the exact cost $g(s)$ from the starting point to node s, and the heuristic estimated cost from node s to the ending point denoted by $h(s)$. Thus, the algorithm begins by analyzing all possible paths in detail from the starting point by successively selecting the next node s with the lowest total cost $J = g(s) + h(s)$, as illustrated in Figure 3. This approach leads to computational efficiency by bypassing the examination of paths deemed too expensive, thus saving computational time since not all possible paths have to be calculated.

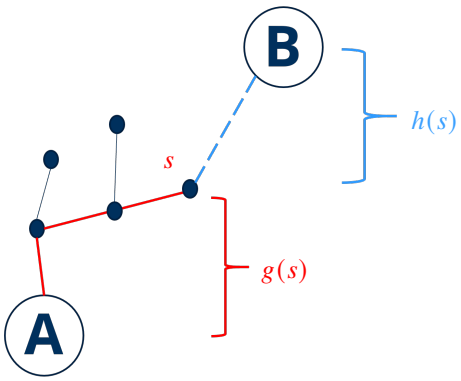

Fig. 3 Illustration of the distinct feature in a A-Star-Algorithm step. The total cost of a path via point s is known by the sum of the exact cost $g(s)$ until point s, and the heuristic estimated cost $h(s)$ from node s to the target

An extension of the basic algorithm enables to consider smoothed flight motions of the UAV. Briefly summarized, we examine three nodes at once to allow heading changes and check if the path respects a minimum turning radius r_{min} and maximum load factor $n_{z,\text{max}}$ as a limit of the UAV. Here, a continuous-curvature path-smoothing algorithm based on cubic Bezier curves including a maximum curvature constraint [19] is used. If the constraints are not fulfilled, the path segment will be neglected. Conversely, if the constraints are satisfied, the combination of the three points is

included for further evaluation of energy-optimal paths. For a detailed description of the extended A-Star Algorithm the reader is referred to [4].

In our case, the exact cost function $g(s)$ includes the energy required, considering the prevailing wind conditions. A specifically developed map tailored for the project is used to calculate the heuristic costs $h(s)$ to improve the performance of the A-Star Algorithm. This map is constructed based on energy distances, where actual distances are transformed to equivalent energy distances, i.e., distances which reflect the energy to fly the distance. The underlying principle is a diffusion-based method for creating density-balanced maps [22]. Updraft influences the energy required the most and is taken as the density value during map creation. A diffusion process controls the density equalization resulting in the creation of a distorted map. A detailed description can be found in [4].

IV. Trajectory Sensitivity

Our previous path optimization assumed perfectly known environmental conditions and accurate path tracking in its cost function. However, real-world operation includes various uncertainties affecting the effective energy savings. Accounting for the impact of uncertainties in the cost function promises less sensitive flight paths. The cost function in this paper explicitly accounts for the additional energy required arising from uncertain environmental conditions. This is accomplished in two steps. First, this section introduces the nominal cost function optimizing the flight trajectory with variable altitude between a predetermined start and end point, as detailed in Section II. Second, several sensitivity components are proposed, each added individually to this nominal cost, to define the exact cost function $g(s)$ in Section III.

A. Nominal Cost Function for Exact Energy Identification

The generic flight path cost function (1) is defined as an integral over the flight path s, which is then discretized in grid points s_i sequentially flown through from start point s_0 until the end point s_N.

$$J = \int_{s_0}^{s_e} A(s)\,\mathrm{ds} = \sum_{i=0}^{N} A_i\,\Delta s_i. \tag{1}$$

The function for the energy required to define the A_i in Eq. (1) contains flight mechanical assumptions that are based on standard literature, such as [23]. To simplify the calculations, the energy supplied by the propulsion system is assumed to be proportional to the thrust force multiplied by the distance covered by the UAV. Hence, A_i is substituted by the thrust T_i, defined by

$$T_i = \frac{u_{\mathrm{UAV,TAS}}}{\sqrt{(u_{\mathrm{UAV,TAS}} - u_{W,i})^2 - v_{W,i}^2}} \cdot (D - \sin(\gamma_i) \cdot mg \cdot n_z)\ . \tag{2}$$

Therein the components are described physically as follows. $\frac{u_{\mathrm{UAV,TAS}}}{\sqrt{(u_{\mathrm{UAV,TAS}} - u_{W,i})^2 - v_{W,i}^2}}$ is the track extension due to horizontal wind with headwind $u_{W,i}$ and the crosswind $v_{W,i}$ at the i-th grid point. $u_{\mathrm{UAV,TAS}}$ is the true airspeed (TAS) of the UAV. The value of D can be determined by the UAV's glide ratio G:

$$D = \frac{L}{G} = \frac{mg}{G} \tag{3}$$

with L as lift force equal to the weight force and the glide ratio G of the fixed-wing UAV. In turning flight with roll angle μ and load factor n_z, D increases to

$$D = \frac{mg}{G} + k \cdot \frac{(mg \cdot n_z)^2}{\frac{\rho}{2} u_{\mathrm{UAV,TAS}}^2 S \cdot cos^2\mu}\ , \tag{4}$$

where S is the wing surface and k the wing contour factor. The flight path angle γ_i is composed of two components: the path component $\gamma_{i,\mathrm{path}}$ and the wind component $\gamma_{i,\mathrm{wind}}$, as given by $\gamma_i = \gamma_{i,\mathrm{path}} + \gamma_{i,\mathrm{wind}}$. The wind component is defined by Eq. (6). The altitude changing component is given by

$$\tan(\gamma_{i,\mathrm{path}}) = \frac{\Delta s_{i,z}}{\Delta s_{i,xy}}\ , \tag{5}$$

where $\Delta s_{i,z}$ is the vertical distance and $\Delta s_{i,xy}$ the horizontal distance to the next point. The wind component $\gamma_{i,\text{wind}}$ is due to upwind condition: For instance, if there is an upwind component, the UAV needs to pitch down to maintain the same flight level. This means that the upwind component $w_{W,i}$ will reduce the flight path angle $\gamma_{i,\text{wind}}$:

$$\sin(\gamma_{i,\text{wind}}) = \frac{w_{W,i}}{u^*_{\text{UAV},i}} \,. \tag{6}$$

This decrease in flight path angle results in a reduction of the required thrust force to maintain steady level flight. A component of the weight vector now supports the force in the direction of flight. All wind components in the nominal cost function are averaged values, e.g. $w_{W,i} = \overline{w_{w,i}}$. Using Eq. (1), the exact cost for flying from start point s_0 to a point s for the minimization of the total energy required in A-Star-Algorithm can be written as:

$$E_{\text{exact},s*} = \sum_{i=0}^{N} E_i = \sum_{i=0}^{N} \Delta s_i \cdot T_i \,. \tag{7}$$

B. Cost Function for Local Drift

So far, the cost function assumes nominal conditions without disturbances and precise path following. However, the presence of gusts or other disturbances may lead to deviations from the optimal path with less favorable wind conditions. To address this issue, we investigate the impact of minor deviations from the flight path, referred to as 'drift' for this study. For this purpose, we compute an energy consumption gradient along the planned flight path at each waypoint. This involve calculating the energy required for the UAV to fly a specified distance perpendicular to both the left and right sides of the path, at a distance of Δd as depicted in Figure 4. The gradients

$$\left(\frac{\Delta E}{\Delta d}\right)_{r,i} = \frac{E(s+\Delta d) - E(s)}{\Delta d} \quad \text{and} \quad \left(\frac{\Delta E}{\Delta d}\right)_{l,i} = \frac{E(s-\Delta d) - E(s)}{\Delta d}, \tag{8}$$

are calculated with the respective energy consumption on the left $E(s+\Delta r)$ and on the right $E(s-\Delta r)$ side of the route from point s to the next testwaypoint.

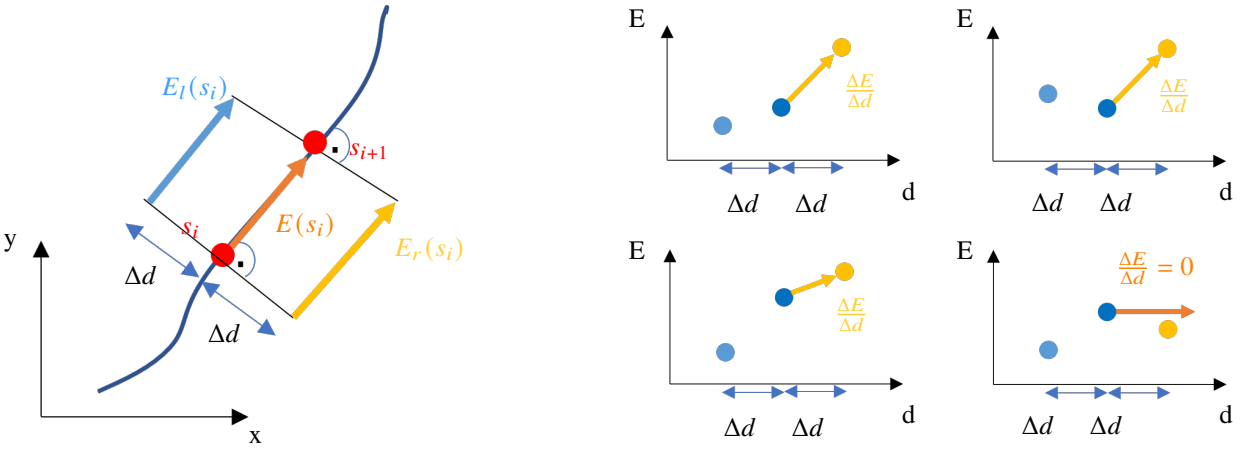

Fig. 4 Local drift at waypoint s_i: Calculating a gradient of energy required, by assuming the UAV flies a specified distance Δd perpendicular to both the left and right sides of the path

The more unfavorable largest gradient is selected to compute the total consumption to increase robustness. If both gradients are negative, the gradient is set to zero. Eq. 9 shows the selection of the gradient in a waypoint.

$$\left(\frac{\Delta E}{\Delta d}\right)_i = \max\left(\left(\frac{\Delta E}{\Delta d}\right)_{r,i}, \left(\frac{\Delta E}{\Delta d}\right)_{l,i}, 0\right) \tag{9}$$

The distance is one grid width of the LES, $\Delta d = 2.5m$. The energy consumption is now calculated by the original path cost E_{path} and the sensitive part $E_{xy-sens}$ as follows:

$$E_i = E_{i,\text{path}} + E_{i,\text{xy-sens}} = E_{i,\text{path}} + \Delta d \cdot \left(\frac{\Delta E}{\Delta d}\right)_i . \tag{10}$$

The gradients are calculated with wind components of averaged values, e.g. $w_{W,i} = \overline{w}_{w,i}$.

C. Cost Function for turbulent Up- and Downwind

Apart from assessing drift, time-depended disturbances are important. Temporal sensitivity along the flight path can be analyzed at individual waypoints. In this context, the time series data from LES results are used from which the time-dependent standard deviation of upwind $\sigma_{i,w(t)}$ is calculated at each wind field point. To account for time-depended up- and downwind, the wind component in z-direction is lowered. The required energy accounts for the reduced upwind by subtracting the standard deviation ($\sigma_{i,w(t)}$) from the averaged value $\overline{w}_{w,i}$. The turbulent-sensitive component $E_{i,\tau\text{-sens}}$ is then:

$$E_{i,\tau\text{-sens}} = E\left(\overline{w}_{w,i} - \sigma_{i,w(t)}\right)_{i,\text{path}} - E\left(\overline{w}_{w,i}\right)_{i,\text{path}} . \tag{11}$$

D. Cost Function for Turbulence Avoidance

This approach involves the identification and avoidance of high turbulence regions along the flight path and includes every wind component in contrast. The turbulence level at a given waypoint s_i is quantified by computing the value of the standard deviations of all wind components:

$$\sigma_i = \sqrt{\sigma^2_{i,u(t)} + \sigma^2_{i,v(t)} + \sigma^2_{i,w(t)}} . \tag{12}$$

A higher σ_i indicates a greater degree of turbulence at point s_i, which should be avoided. Hence, the cost function is determined by:

$$E_{i,\tau\text{-avoid}} = \lambda \cdot \sigma_i \quad \text{and} \quad E_i = E\left(\overline{w_{w,i}}\right)_i + \lambda \cdot \sigma_i , \tag{13}$$

where λ is set to $1\frac{\text{kg·m}}{\text{s}}$. The term $\lambda \cdot \sigma_i$ ensures physical consistency and $\lambda = 1\frac{\text{kg·m}}{\text{s}}$ leads to the same order of magnitude as the turbulent sensitive component $E_{i,\tau\text{-sens}}$ of Section IV.C.

E. Combinations of Cost Functions

The final variant of cost function involves the combination of two methodologies from above. The nominal function is expanded to consider two sensitive components. To prevent immoderate influence from the combined components against the nominal costs and ensure balanced weighting, a factor of 0.5 is applied to each. A combination of drift and turbulent sensitivity is chosen, since the proximity of turbulence avoidance and turbulent sensitivity exhibits familiar behaviour. Therefore, the exact cost calculation is proposed as

$$E_i = E\left(\overline{w_{w,i}}\right)_i + 0.5 \cdot E_{i,\text{xy-sens}} + 0.5 \cdot E_{i,\tau\text{-sens}} . \tag{14}$$

Note that alternative combinations could also be chosen.

V. Results of Trajectory Optimization and Sensitivity

In this section, we present the results of the flight path optimization using the cost function proposed in Section IV.A and their sensitive parts in Section IV.B to IV.E. The optimization was performed for two different scenarios as specified in Section II, where each scenario involved one of the two track directions and a freestream wind speed of 6.5 m/s. For each scenario and each sensitivity, three optimal trajectories were computed. First, using the nominal cost function of Eq.(7). Second, adding one of the three sensitive component $E_{i,\text{xy-sens}}$, $E_{i,\tau\text{-sens}}$, or $E_{i,\tau\text{-avoid}}$ to Eq.(7). Third, using a simple shortest path optimization described by $J_{\text{exact},i} = \sum_{i=0}^{N} \Delta s_i$ and the direct distance as heuristic function. The A-Star-Algorithm was used for optimization in all cases. Table 1 summarizes the different optimizations. Note that the energy optimal trajectory without sensitives is the same each sensitivity comparison, denoted by the *.

Table 1 Summary of calculations applied with A*

Trajectory Sensitivity	...in Optimization Process	...only in results
Shortest way *	$J_i = \Delta s_i$	$E_i = E\left(\overline{w}_{w,i}\right)_i + E_{i,\text{xy-sens}}$
Energy-optimal nominal *	$E_i = E\left(\overline{w}_{w,i}\right)_i + 0$	$E_i = E\left(\overline{w}_{w,i}\right)_i + E_{i,\text{xy-sens}}$
Local Drift	$E_i = E\left(\overline{w}_{w,i}\right)_i + E_{i,\text{xy-sens}}$	$E_i = E\left(\overline{w}_{w,i}\right)_i + E_{i,\text{xy-sens}}$
Shortest way *	$J_i = \Delta s_i$	$E_i = E\left(\overline{w_{w,i}}\right)_i + E_{i,\tau\text{-sens}}$
Energy-optimal nominal *	$E_i = E\left(\overline{w}_{w,i}\right)_i + 0$	$E_i = E\left(\overline{w}_{w,i}\right)_i + E_{i,\tau\text{-sens}}$
Turbulence	$E_i = E\left(\overline{w}_{w,i}\right)_i + E_{i,\tau\text{-sens}}$	$E_i = E\left(\overline{w}_{w,i}\right)_i + E_{i,\tau\text{-sens}}$
Shortest way *	$J_i = \Delta s_i$	$E_i = E\left(\overline{w}_{w,i}\right)_i + E_{i,\tau\text{-avoid}}$
Energy-optimal nominal *	$E_i = E\left(\overline{w}_{w,i}\right)_i + 0$	$E_i = E\left(\overline{w}_{w,i}\right)_i + E_{i,\tau\text{-avoid}}$
Turbulence Avoidance	$E_i = E\left(\overline{w}_{w,i}\right)_i + E_{i,\tau\text{-avoid}}$	$E_i = E\left(\overline{w}_{w,i}\right)_i + E_{i,\tau\text{-avoid}}$
Shortest way *	$J_i = \Delta s_i$	$E_i = E\left(\overline{w}_{w,i}\right)_i + 0.5 \cdot E_{i,\text{xy-sens}} + 0.5 \cdot E_{i,\tau\text{-sens}}$
Energy-optimal nominal *	$E_i = E\left(\overline{w}_{w,i}\right)_i + 0$	$E_i = E\left(\overline{w}_{w,i}\right)_i + 0.5 \cdot E_{i,\text{xy-sens}} + 0.5 \cdot E_{i,\tau\text{-sens}}$
Combination	$E_i = E\left(\overline{w}_{w,i}\right)_i + 0.5 \cdot E_{i,\text{xy-sens}} + 0.5 \cdot E_{i,\tau\text{-sens}}$	$E_i = E\left(\overline{w}_{w,i}\right)_i + 0.5 \cdot E_{i,\text{xy-sens}} + 0.5 \cdot E_{i,\tau\text{-sens}}$

The energy required for each scenario is quantified and presented in terms of energy savings in percentage. This percentage is calculated as

$$p = \frac{E_{\text{shortest way}} - E_{\text{energy opt.}}}{E_{\text{shortest way}}} \cdot 100\% \,, \tag{15}$$

where $E_{\text{shortest way}}$ and $E_{\text{energy opt.}}$ are the energy required without sensitive parts for the shortest path and the energy-optimal path, respectively. If the sensitive parts are included, the notation is $p_{\text{-sens}}$, calculated with the equation in the "only in results"-column of Table 1. All paths exhibits minimal variations in altitude in the range of ±0 78m, similar to those observed in [4]. They occur for main reason to fly over the terraced houses or for low-level flight to avoid turbulence.

A. Results of South-North-Track

Table 2 and Figure 5 presents the results of local drift, flying South to North. Figure 5 shows different flight paths. The orange line represents the shortest path. The blue dashed line the energy-optimal without the sensitive part, and the blue line shows the path with the lowest energy required including the sensitive part. The flight paths obtained from the optimization process exhibit interesting characteristics that merit further investigation. Firstly, the solely energy optimized path closely follows the rooftops of the buildings. This is due to the presence of strong upwinds in front of buildings. These upwinds result in lower energy consumption when flying alongside them with the wind perpendicular to the building's orientation. This phenomenon is akin to ridge lift, which is exploited by sail planes in mountainous regions. Secondly, these regions tend to be more sensitive to local drift if drift occurs, see Table 2. Hence, the optimized path including drift sensitivity is completely different and leads through areas with lower sensitive parts. Thirdly, the shortest way has a relative small sensitive part and keeps a distance to the buildings. If drift occurs, energy will only be saved if the local drift was explicitly respected in the optimization. Hence, a more robust trajectory is provided.

Table 2 Results of local drift

Cost function	$E\left(\overline{w}_{w,i}\right)_i$ in J	p	$E_{i,\text{xy-sens}}$ in J	$E\left(\overline{w}_{w,i}\right)_i + E_{i,\text{xy-sens}}$ in J	$p_{\text{xy-sens}}$
Shortest way	314.4		9.8	324.2	
Energy-optimal nominal	247.6	-21.2%	84.3	331.9	+2.4%
Local Drift	289.2	-8.0%	12.3	301.5	-7.0%

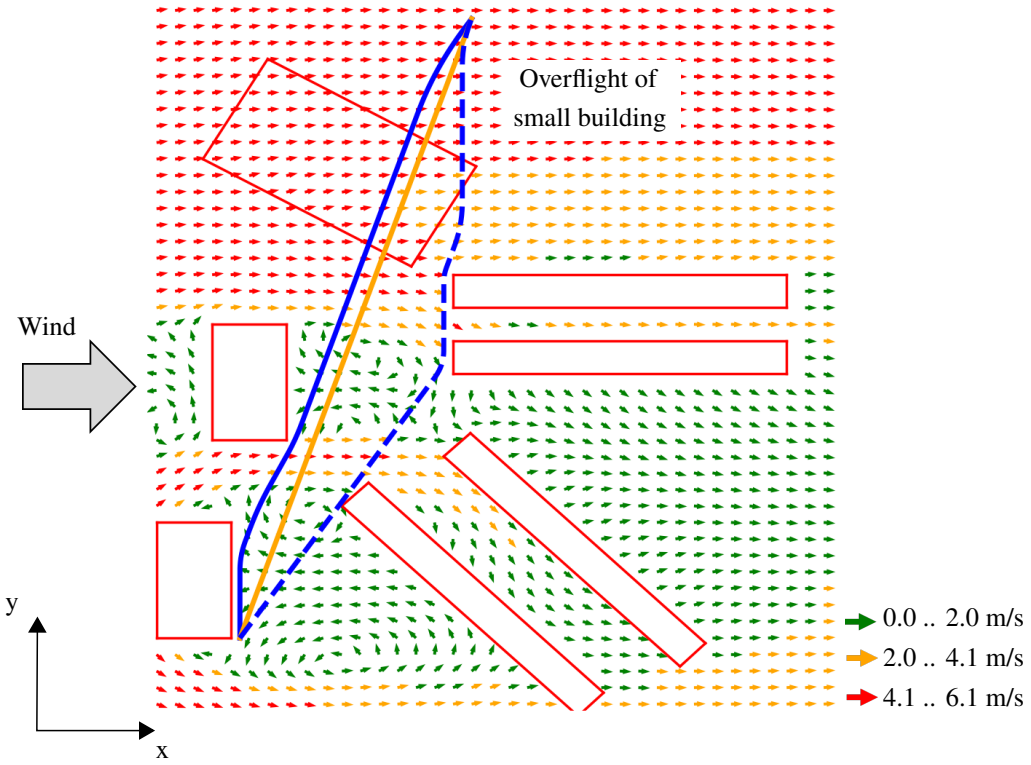

Fig. 5 Flight path for $u_{W\infty} = 6.5$m/s with wind field in height of 20 m(⟶), buildings (——), shortest way (——), energy optimized path after A-Star-Algorithm without trajectory sensitivity (- - -), and with local drift-sensitivity (——), flying South to North

The turbulence component results in comparatively minor deviations compared to the drift sensitivity, as illustrated in Figure 6-a). Hence, the energy savings compared to the shortest path are only marginally reduced when turbulence sensitivity is incorporated. The sensitive components are in the same magnitude across all paths in this scenario, as shown in the $E_{i,\tau\text{-sens}}$-column in Table 3. Thus, it becomes evident that integrating turbulence sensitivity into the optimization process yields to further energy savings, if the reduced upwind always occurs. Despite the reduction in upwind, the optimization still results in flight towards the upwind zone in front of the terraced houses.

Table 3 Results of turbulence-sensitivity

Cost function	$E\left(\overline{w}_{w,i}\right)_i$ in J	p	$E_{i,\tau\text{-sens}}$ in J	$E\left(\overline{w}_{w,i}\right)_i + E_{i,\tau\text{-sens}}$ in J	$p_{\tau\text{-sens}}$
Shortest way	314.4		173.4	487.8	
Energy-optimal nominal	247.6	-21.2%	168.5	416.1	-14.7%
Turbulence	256.1	-18.5%	156.6	412.7	-15.4%

Applying the turbulence avoidance component, which also accounts for the standard deviation of horizontal wind, significantly alters the flight path. Figure 6-b) shows that the path now leads behind the high-rise buildings, where turbulence is comparatively low. These high-rise buildings have a height of 50m and the altitude of the UAVs is approximately 20m. At this altitude, eddies resulting from the flow around the buildings are less distinctive than the ones closer to the roof. Again, integrating the turbulence avoidance component into the optimization process promises further energy savings, if avoidance is necessary. Table 4 quantifies this relation.

Table 5 summarizes the results for combined drift and turbulence components. The reduction in savings due to uncertainty consideration is comparable to the outcomes observed when only using the drift component alone. However,

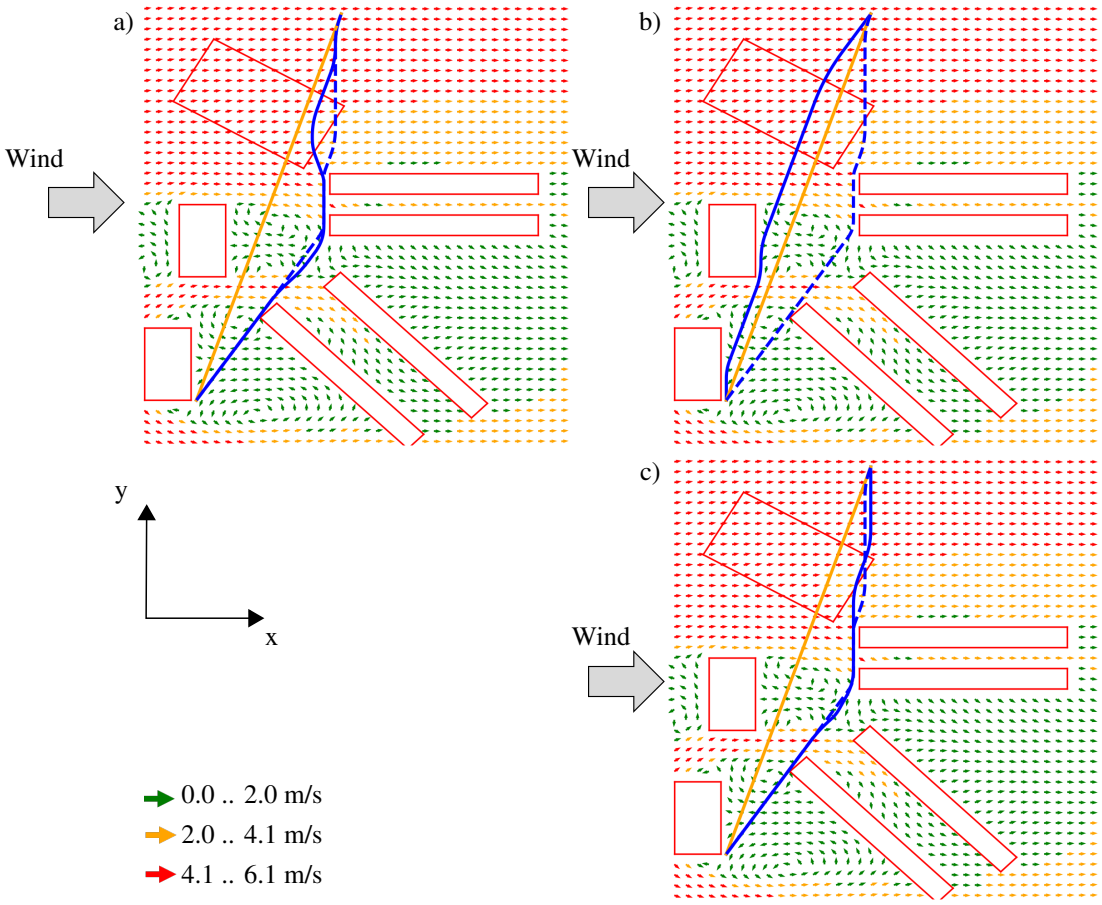

Fig. 6 Flight path for $u_{W\infty}$ = 6.5m/s with wind field in height of 20 m(⟶), buildings (——), shortest way (——), energy optimized path after A-Star-Algorithm without trajectory sensitivity (- - -), and with a) turbulence-sensitivity, b) turbulence-avoidance, c) combination of drift and turbulence-sensitivity (each ——), flying South to North

Table 4 Results of turbulence-avoidance

Cost function	$E\left(\overline{w}_{w,i}\right)_i$ in J	p	$E_{i,\tau\text{-avoid}}$ in J	$E\left(\overline{w}_{w,i}\right)_i + E_{i,\tau\text{-avoid}}$ in J	$p_{\tau\text{-avoid}}$
Shortest way	314.4		221.5	535.9	
Energy-optimal nominal	247.6	-21.2%	260.6	508.2	-5.2%
Turbulence Avoidance	287.5	-8.6%	203.3	490.8	-8.4%

the resulting flight path differs completely. Figure 6-c) shows that the path is aligned with the trajectory generated by the nominal optimization. It also differs just slightly to that one from the turbulence component optimization. It can be deduced that the turbulence component, with its higher values, has more significant influence on the overall objective. However, the resulting path comes up with lower energy savings.

B. Results of East-West-Track

The results from the East-West track exhibit similar trends. These various paths are illustrated in Figure 7-a)-d) with unchanged color code. The shortest path no longer follows a straight line due to the presence of a terraced house obstructing the direct route, as well as the constrained waypoint connections, described in II. Trajectories of drift- (a), turbulence-sensitivity (b), and their combination (d) exhibit less deviations from the purely energy-efficient trajectory. Notably, the time-dependent airflow has a bigger fluctuation along the facade of the terraced house. Hence, the trajectory sensitive to turbulence diverges above the building, rather than traversing near the rooftop corner. In contrast, the

Table 5 Results of sensitivity combination

Cost function	$E\left(\overline{w}_{w,i}\right)_i$ in J	p	$E_{i,\text{xy-}\tau\text{-comb}}$ in J	$E\left(\overline{w}_{w,i}\right)_i + E_{i,\text{xy-}\tau\text{-comb}}$ in J	$p_{\text{xy-}\tau\text{-comb}}$
Shortest way	314.4		91.6	406.0	
Energy-optimal nominal	247.6	-21.2%	126.4	374.0	-7.9%
Combination	254.7	-19.0%	105.1	359.8	-11.4%

turbulence-avoidance path (c) differs significantly, as it yields along the high-rise buildings. This behavior is consistent within the South-North track. Turbulence is comparatively less prevalent behind the towers in this height. The tables in the appendix (6-9) present the quantitative results of the energy savings. In contrast to the results from the South-North track, even the nominal energy-efficient path without accounting uncertainties, has energy savings if drift occurs. Again, integrating each component or their combination into the optimization process promises further energy savings if the anticipated uncertainties appear and less sensitivity. Moreover, the sensitive components in the East-West track exceeds that of the South-North track, particularly noticeable in the case of the shortest path. This observation suggests that flying for extended duration close to buildings increases path sensitivity.

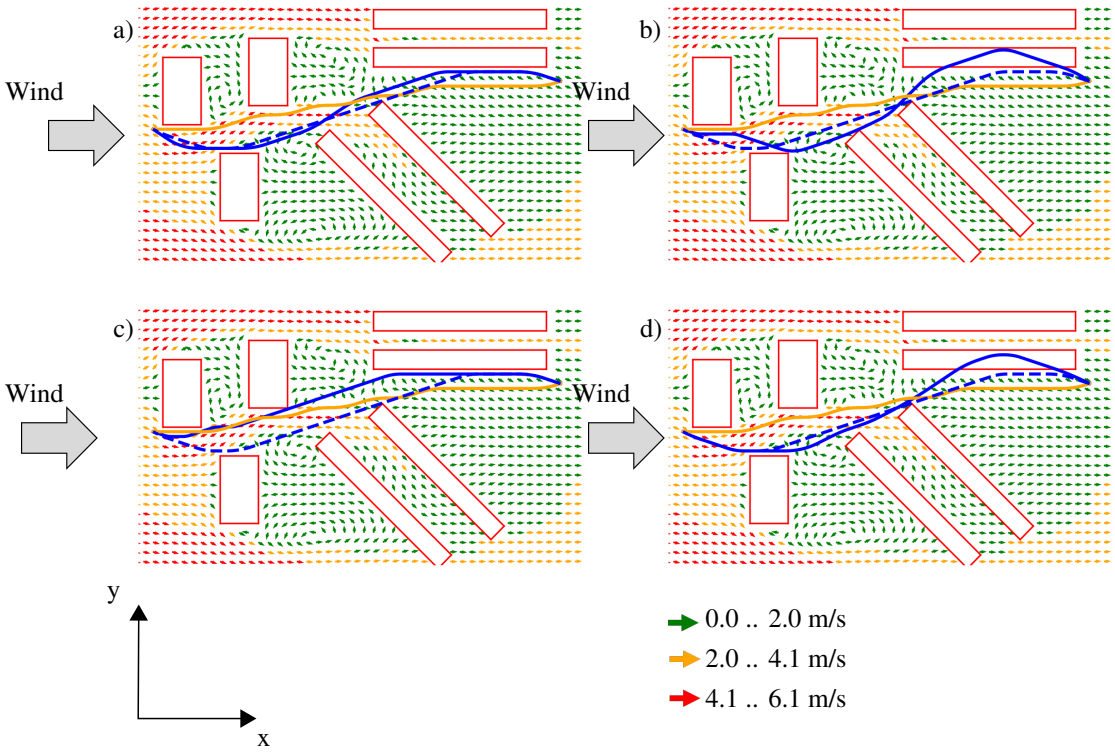

Fig. 7 Flight path for $u_{W\infty}$ = 6.5m/s with wind field in height of 20 m(⟶), buildings (——), shortest way (——), energy optimized path after A-Star-Algorithm without trajectory sensitivity (- - -), and with a) drift-sensitivity, b) turbulence-sensitivity, c) turbulence-avoidance, d) combination of drift and turbulence-sensitivity (each ——), flying East to West

VI. Conclusion

We introduced an approach aimed at optimizing the energy efficiency of 3D flight trajectories for delivery UAVs while considering uncertainties. The methodology applied a realistic city model including a time-dependent wind field to facilitate the path optimization process. Our results underscored the effectiveness of integrating sensitivities into the

A-Star Algorithm to optimize trajectories robust with respect to uncertainties. Particularly, our findings demonstrate consistent energy savings across various types of uncertainties, resulting in a significant reduction in energy consumption under anticipated conditions. These enhancements make the energy-efficient trajectories more robust and improve the quality of the results obtained.

In the future, our focus will shift towards incorporating the actual position of the UAV in real-time. While our current work considers the worst upwind condition around each waypoint, future efforts will integrate the UAV's control system with a path-following controller. This integration will enable the UAV to adapt its flight path dynamically in response to time-dependent uncertainties obtained through Monte Carlo simulations. Hence, uncertainties can be addressed in a more realistic and responsive manner.

Appendix

Table 6 Results of local drift, flying East to West

Cost function	$E\left(\overline{w}_{w,i}\right)_i$ in J	p	$E_{i,\text{xy-sens}}$ in J	$E\left(\overline{w}_{w,i}\right)_i + E_{i,\text{xy-sens}}$ in J	$p_{\text{xy-sens}}$
Shortest way	504.5		69.5	574	
Energy-optimal nominal	418.1	-17.1%	74.2	492.3	-14.2%
Local Drift	426.4	-15.5%	35.4	461.8	-19.5%

Table 7 Results of turbulence-sensitivity, flying East to West

Cost function	$E\left(\overline{w}_{w,i}\right)_i$ in J	p	$E_{i,\tau\text{-sens}}$ in J	$E\left(\overline{w}_{w,i}\right)_i + E_{i,\tau\text{-sens}}$ in J	$p_{\tau\text{-sens}}$
Shortest way	504.5		316.6	821.1	
Energy-optimal nominal	418.1	-17.1%	272.4	690.5	-15.9%
Turbulence	442.8	-12.2%	208.6	651.4	-20.7%

Table 8 Results of turbulence-avoidance, flying East to West

Cost function	$E\left(\overline{w}_{w,i}\right)_i$ in J	p	$E_{i,\tau\text{-avoid}}$ in J	$E\left(\overline{w}_{w,i}\right)_i + E_{i,\tau\text{-avoid}}$ in J	$p_{\tau\text{-avoid}}$
Shortest way	504.5		301	805.5	
Energy-optimal nominal	418.1	-17.1%	303.5	721.6	-10.4%
Turbulence Avoidance	456.4	-9.5%	242.8	699.2	-13.2%

Table 9 Results of sensitivity combination, flying East to West

Cost function	$E\left(\overline{w}_{w,i}\right)_i$ in J	p	$E_{i,\text{xy-}\tau\text{-comb}}$ in J	$E\left(\overline{w}_{w,i}\right)_i + E_{i,\text{xy-}\tau\text{-comb}}$ in J	$p_{\text{xy-}\tau\text{-comb}}$
Shortest way	504.5		193.05	697.55	
Energy-optimal nominal	418.1	-17.1%	173.3	591.4	-15.2%
Combination	427.3	-15.3%	136.2	563.5	-19.2%

Acknowledgments

This research was funded by the German Federal Ministry for Economic Affairs and Climate Action under grant number 20D2106C. The responsibility for the content of this paper is with its authors. The financial support is gratefully acknowledged.

References

[1] Kirschstein, T., "Comparison of energy demands of drone-based and ground-based parcel delivery services," *Transportation Research Part D: Transport and Environment **78**, Article 102209*, 2020. doi:10.1016/j.trd.2019.102209.

[2] Rienecker, H., Hildebrand, V., and Pfifer, H., "Energy optimal flight path planing for unmanned aerial vehicle in urban environments," *Proceedings of the 2022 CEAS EuroGNC conference*, CEAS, Berlin, Germany, 2022. CEAS-GNC-2022-031.

[3] Rienecker, H., Hildebrand, V., and Pfifer, H., "Energy optimal 3D flight path planning for unmanned aerial vehicle in urban environments," *CEAS Aeronautical Journal*, Vol. 14, 2023, pp. 621–636. doi:10.1007/s13272-023-00666-x.

[4] Rienecker, H., Hildebrand, V., and Pfifer, H., "Energy Optimal Flight Path Planning for Unmanned Aerial Vehicles in Urban Environments Based on a Novel Energy-Distance Map," *Proceedings of the 2024 AIAA SciTech conference*, AIAA, Orlando, USA, 2024.

[5] Pang, B., Low, K. H., and Lv, C., "Adaptive conflict resolution for multi-UAV 4D routes optimization using stochastic fractal search algorithm," *Transportation Research Part C: Emerging Technologies*, Vol. 139, 2022, p. 103666. doi:https://doi.org/10.1016/j.trc.2022.103666, URL https://www.sciencedirect.com/science/article/pii/S0968090X22001097.

[6] González-Arribas, D., Soler, M., and Sanjurjo-Rivo, M., "Robust Aircraft Trajectory Planning Under Wind Uncertainty Using Optimal Control," *Journal of Guidance, Control, and Dynamics*, Vol. 41, No. 3, 2018, pp. 673–688. doi:10.2514/1.G002928.

[7] Dias, F. H., and Rey, D., "Robust aircraft conflict resolution under trajectory prediction uncertainty," , 2022. doi:https://doi.org/10.1016/j.orl.2022.07.010, URL https://www.sciencedirect.com/science/article/pii/S0167637722000943.

[8] Goel, S., Kealy, A., and Lohani, B., "Development and Experimental Evaluation of a Low-Cost Cooperative UAV Localization Network Prototype," *Journal of Sensor and Actuator Networks*, Vol. 7, 2018. doi:10.3390/jsan7040042.

[9] Wolf, M. T., Blackmore, L., Kuwata, Y., Fathpour, N., Elfes, A., and Newman, C., "Probabilistic motion planning of balloons in strong, uncertain wind fields," *2010 IEEE International Conference on Robotics and Automation*, 2010, pp. 1123–1129. doi:10.1109/ROBOT.2010.5509135.

[10] Al-Sabban, W. H., Gonzalez, L. F., and Smith, R. N., "Wind-energy based path planning for Unmanned Aerial Vehicles using Markov Decision Processes," *2013 IEEE International Conference on Robotics and Automation*, 2013, pp. 784–789. doi:10.1109/ICRA.2013.6630662.

[11] Kay, N. J., Richards, P. J., and Sharma, R. N., "Influence of Turbulence on Cambered and Symmetrical Airfoils at Low Reynolds Numbers," *AIAA Journal*, Vol. 58, No. 5, 2020, pp. 1913–1925. doi:10.2514/1.J058822, URL https://doi.org/10.2514/1.J058822.

[12] Wang, B. H., Wang, D. B., Ali, Z. A., Ting, B. T., and Wang, H., "An overview of various kinds of wind effects on unmanned aerial vehicle," *Measurement and Control*, Vol. 52, No. 7-8, 2019, pp. 731–739. doi:10.1177/0020294019847688, URL https://doi.org/10.1177/0020294019847688.

[13] Maronga, B., Gryschka, M., Heinze, R., Hoffmann, F., Kanani-Sühring, F., Keck, M., Ketelsen, K., Letzel, M. O., Sühring, M., and Raasch, S., "The Parallelized Large-Eddy Simulation Model (PALM) version 4.0 for atmospheric and oceanic flows: model formulation, recent developments, and future perspectives," *Geoscientific Model Development*, Vol. 8, No. 8, 2015, pp. 2515–2551. doi:10.5194/gmd-8-2515-2015.

[14] Frey, J., Rienecker, H., Schubert, S., Hildebrand, V., and Pfifer, H., "Wind Tunnel Measurement of the Urban Wind Field for Flight Path Planning of Unmanned Aerial Vehicles," *Proceedings of the 2024 AIAA SciTech conference*, AIAA, Orlando, USA, 2024.

[15] Rosenow, J., Lindner, M., and Fricke, H., "Assessment of air traffic networks considering multi-criteria targets in network and trajectory optimization," *Deutscher Luft- und Raumfahrtkongress 2015*, DGLR, Rostock, Germany, 2015.

[16] Junwei, Z., and Jianjun, Z., "Path Planning of Multi-UAVs Concealment Attack Based on New A Method," *2014 Sixth International Conference on Intelligent Human-Machine Systems and Cybernetics*, IEEE, New York City, United States, 2014, pp. 401–404. doi:10.1109/ihmsc.2014.198.

[17] Garcia, M., Viguria, A., and Ollero, A., "Dynamic Graph-Search Algorithm for Global Path Planning in Presence of Hazardous Weather," *Journal of Intelligent & Robotic Systems*, Vol. 69, 2012, p. 285–295. doi:10.1007/s10846-012-9704-7.

[18] Mandloi, D., Arya, R., and Verma, A. K., "Unmanned aerial vehicle path planning based on A$*$ algorithm and its variants in 3d environment," *International Journal of System Assurance Engineering and Management*, Vol. 12, No. 5, 2021, pp. 990–1000. doi:10.1007/s13198-021-01186-9.

[19] Yang, K., and Sukkarieh, S., "3D smooth path planning for a UAV in cluttered natural environments," *2008 IEEE/RSJ International Conference on Intelligent Robots and Systems*, IEEE, New York City, United States, 2008, pp. 794–800. doi:10.1109/iros.2008.4650637.

[20] "PWOne," Phoenix-Wings GmbH, 2022. URL `https://phoenix-wings.de/pwone/`, accessed 2021-10-18.

[21] "VDI 3783 Part 12, Environmental meteorology: Physical modelling of flow and dispersion processes in the atmospheric boundary layer, Application of wind tunnels," , Jul. 2022. URL `http://www.vdi.de/3783-12`.

[22] Gastner, M. T., and Newman, M. E. J., "Diffusion-based method for producing density-equalizing maps," *Proceedings of the National Academy of Sciences*, Vol. 101, No. 20, 2004, pp. 7499–7504. doi:10.1073/pnas.0400280101.

[23] McClamroch, N. H., *Steady Aircraft Flight and Performance*, Princeton University Press, Princeton, 2011. ISBN: 9781680159097.